Characterization of Sierpinski carpet optical antenna at visible and near-infrared wavelengths

2014 New J. Phys. 16 093024

(http://iopscience.iop.org/1367-2630/16/9/093024)

New Journal of Physics
The open access journal at the forefront of physics
Deutsche Physikalische Gesellschaft DPG | IOP Institute of Physics

Characterization of Sierpinski carpet optical antenna at visible and near-infrared wavelengths

Ting Lee Chen[1], Dirk Jan Dikken[1], Jord C Prangsma[1,2], Frans Segerink[1] and Jennifer L Herek[1]

[1] Optical Sciences Group, MESA+ Institute for Nanotechnology, University of Twente, 7500 AE Enschede, The Netherlands
[2] Nanobiophysics, MESA+ Institute for Nanotechnology, University of Twente, 7500 AE Enschede, The Netherlands
E-mail: J.L.Herek@utwente.nl

Received 17 March 2014, revised 16 July 2014
Accepted for publication 1 August 2014
Published 19 September 2014
New Journal of Physics **16** (2014) 093024
doi:10.1088/1367-2630/16/9/093024

Abstract

We present fabrication, characterization, and simulation results on an optical antenna inspired by the Sierpinski carpet fractal geometry for operation in the visible and near-infrared wavelength regions. Measurements and simulations of the far-field scattering efficiency indicate a broadband optical response. Two-photon photoluminescence images provide maps of the near-field intensity distribution, from which we extract an enhancement factor of ~70. To explore the effect of morphology on the optical response of a large assembly of particles, we also present results on an arbitrarily chosen pseudo-random configuration as well as a periodic array.

Keywords: optical antenna, fractal, plasmonic, broadband, nanostructure

Introduction

Plasmonic optical antennas use localized surface plasmon resonances in metal nanostructures to interface efficiently between propagative light and localized electromagnetic fields [1–3]. At resonance, the optical extinction cross section of a metal nanoparticle can be significantly larger than its physical cross section. This property can be used to create efficient absorbers [4] or to

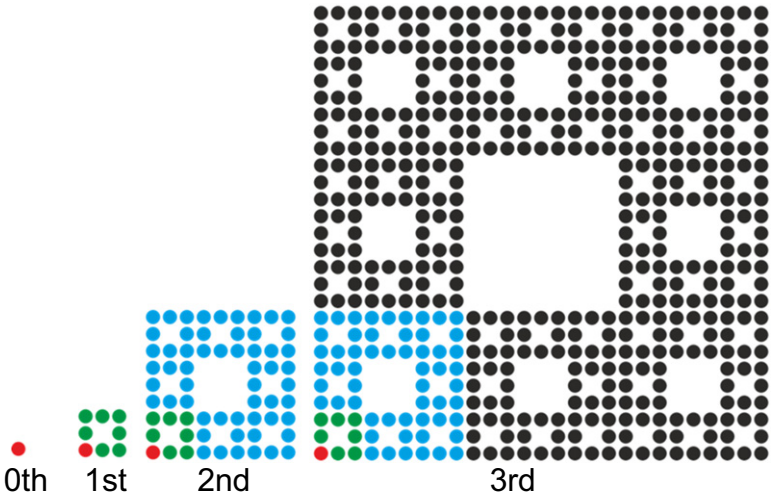

Figure 1. The Sierpinski carpet inspired fractal structure investigated in this paper. Starting from 0th order—a monomer (red circle), then a 3×3 grid with the central monomer removed (1st order) and so forth (2nd and 3rd order).

increase the optical path length of light traveling through a semiconductor substrate [5]. Additionally, metal nanostructures can lead to enhanced near-field intensities and confine light energy within subwavelength regions in space. Therefore, optical antennas have attracted a lot of attention in light harvesting-related applications such as photo detection [6, 7], solar cells [5, 8], and surface-enhanced Raman spectroscopy [9].

Progress in fabrication technologies has facilitated the development of optical antennas in a wide range of different sizes and shapes. Metal nano-rods, dipole and bowtie optical antennas can be fabricated with dimensions down to several tens of nanometers, allowing precise tuning of optical properties such as the resonant wavelength [10, 11]. To create optical antennas with a broadband response, pseudo-random, periodic, and aperiodic metal nanostructures have recently been studied [12–15]. Contrary to the radio-frequency range where broadband antennas based on fractal geometries have already been used for 'frequency independent' antenna design [16], in the optical regime broadband fractal optical antennas are relatively unexplored [17–19]. Here we explore the optical analogue of the radio-frequency fractal antenna and investigate the optical properties of a metal particle nanostructure based on fractal geometry.

Sample design and fabrication

Fractal geometries, patterns based on self-similarity, exist in a large variety of shapes and forms [20]. Figure 1(b) shows one such fractal geometry, whose design is inspired by a well-known classic of fractals, the 'Sierpinski carpet' [21]. Fractal geometries can be built up using a simple design rule. We chose to start from a circle as the basic element. This circle is copied into an array of three by three, and the central one is removed, creating the first order unit of the structure. The same procedure is recursively applied to construct the next order of the fractal pattern, as figure 1 shows. With the continuation of this simple iterative process, for which the first three steps are visualized, the Sierpinski carpet-inspired structure shows an increasing complexity in periodicity. Similar geometries were studied by Volpe *et al* [18], who suggested

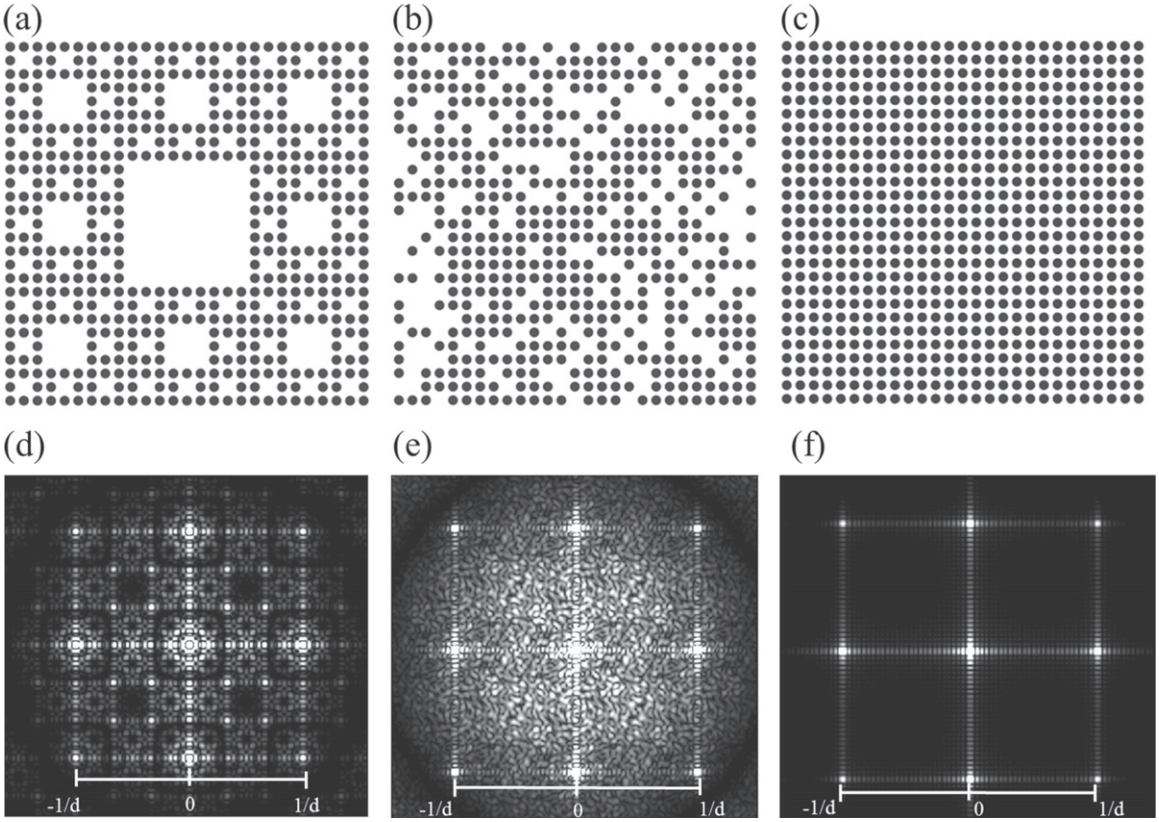

Figure 2. Schematics (a)–(c) and their Fourier spectra amplitude (d)–(f) of Sierpinski carpet, pseudo-random and periodic structures. In the scale bar, d is the center-to-center monomer distance of the Sierpinski carpet, pseudorandom and periodic structures. The ratio of the monomer diameter to the distance d is 8:11.

their use as broadband optical antennas. Note that an essential difference between the structures we study here and the classical Sierpinski carpet is that the latter consists of one continuous material with holes, whereas our design is constructed from isolated monomers arranged in the characteristic pattern. Nevertheless, the clear similarity merits the labeling of our structure as a Sierpinski carpet antenna.

In this article we investigate the far-field scattering spectrum and near-field intensity enhancement of the Sierpinski carpet gold nanostructure, both experimentally and numerically. In addition, we employ a pseudo-random and a periodic gold nanostructure to explore the influence of morphology on the optical properties of these large arrays of gold particles. Scattering spectra of the gold nanostructures were obtained by white-light dark field microscopy, and two-photon photoluminescence (TPPL) microscopy was used to visualize the near-field intensity enhancement of the Sierpinski carpet, pseudo-random, and periodic gold nanostructures.

The geometric patterns of the three samples are shown in figure 2, both in real space (a)–(c) and k-space (d)–(f). A total of 512 individual monomers are used to create the Sierpinski carpet pattern and pseudo-random distribution shown in (a) and (b), respectively, corresponding to 70% of the available sites in the 27×27 matrix. For the periodic structure (c), all 729 lattice sites are covered. Of course, the pseudo-random pattern shown in figure 2(b) is just one

realization (out of $>10^{100}$ possible configurations!) in which the 512 monomers are distributed randomly on the lattice. It is chosen arbitrarily for its lack of 'self-similarity' relative to the Sierpinski carpet and periodic patterns, and thereby affords an opportunity for comparison. Nevertheless, the reader is cautioned against generalizing the results from what might just be lucky chance and not characteristic of all random configurations.

To better compare the three morphologies, we switch to k-space by calculating their spatial Fourier transforms. The Fourier spectra amplitudes are plotted in figures 2(d)–(f), directly below their corresponding patterns (a)–(c). Primary peaks in the Fourier spectra amplitude image of the three configurations reflect the square lattice structure, as best seen in the fully periodic case (f). In the Sierpinski carpet morphology (d), besides the primary peaks, other distinct peaks are observed, corresponding to regular periodicities present in the carpet. With the increase of the iterative order of the Sierpinski carpet structure, the Fourier spectra amplitude will have more distinct points (data not shown). In contrast, the reciprocal vectors in the pseudo-random structure (e) are more evenly and continuously distributed as compared with that from the Sierpinski carpet structure. The symmetry in the Sierpinski carpet morphology results in a regular and highly symmetric distribution of its reciprocal vectors, filling in the regions between the primary peaks of the periodic morphology. The pseudo-random morphology only shows a point symmetry with respect to the origin.

Fabrication

To fabricate our samples, we used Focused Ion Beam (FIB) milling (FEI Nova 600 dual beam) to carve nanostructures directly on single-crystalline gold flakes [22] that were chemically synthesized by the procedure described in [23].

We deposited single crystalline gold flakes onto a glass substrate with a 100 nm ITO coating. The flake was pre-thinned to the thickness of ~40 nm with FIB milling. In the FIB milling process, the acceleration voltage was 30 kV, and the Ga-ion current was 1.5 pA. Structures were milled using 30 passes of the ion beam. In [22], it was shown by energy-dispersive x-ray analysis that the implantation of Ga-ions into gold nanostructures in the FIB milling process is negligible. Therefore, we can assume that the optical properties of the substrate and the gold itself are not degraded after the FIB milling process. Figure 3 shows fabrication results of the Sierpinski carpet, pseudo-random, and periodic gold nanostructures on a single crystalline gold flake. All nanostructures have the same monomer size of 80 ± 8 nm diameter and 40 ± 5 nm thickness; the gap distance between monomers is 30 ± 11 nm. Monomer numbers for the Sierpinski carpet and pseudo-random nanostructures are both 512, corresponding to 70% of available sites in the 27×27 matrix; in the periodic nanostructure all 729 sites are occupied. The monomer size was chosen such that the fabricated nanostructures exhibit optical response in the spectral detection range of our acquisition system (400–900 nm).

Far-field optical properties

Methods

To measure the far-field scattering properties of the structures, we employed a home-built dark-field spectrometer setup as shown schematically in figure 4(a). White light from a Xenon Arc lamp (Oriel 71213, Newport) is sent into a microscope (IX71, Olympus) and focused onto

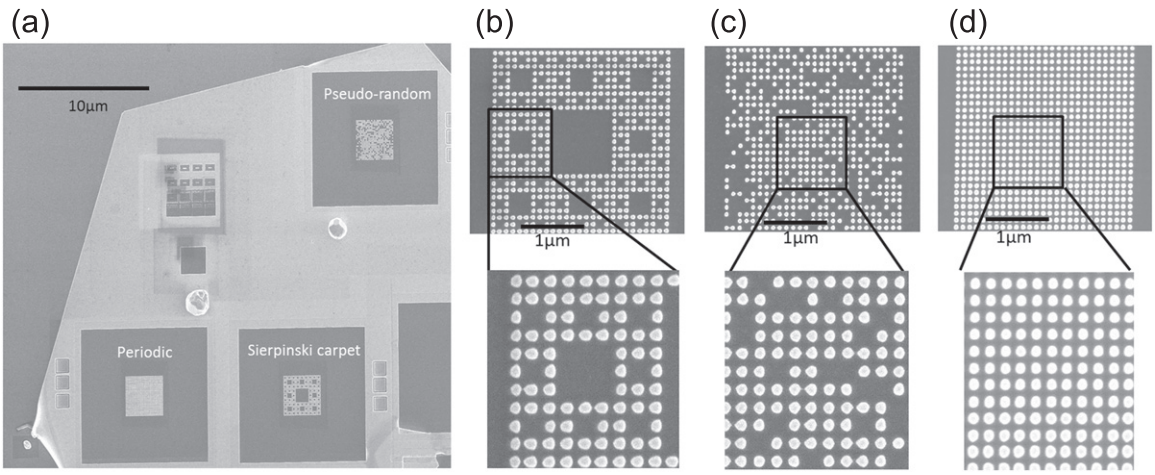

Figure 3. Scanning electron microscope (SEM) images of samples fabricated by FIB milling: (a) fabrication of Sierpinski carpet, pseudo-random and periodic nanostructures on a single crystalline gold flake, (b) the Sierpinski carpet nanostructure, (c) the pseudo-random nanostructure and (d) the periodic nanostructure. The monomer size and gap distance between monomers for all samples are 80 nm diameter, 40 nm height, and 30 nm gap distance.

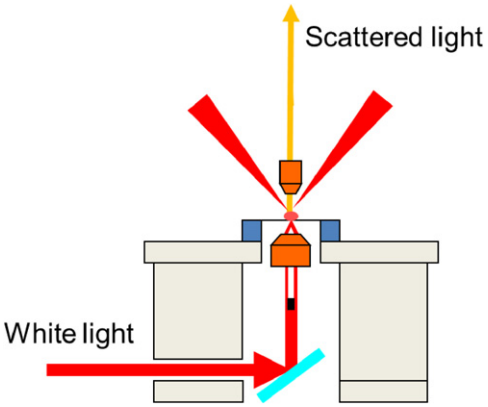

Figure 4. A schematic of white-light dark field microscopy. Note the inclusion of a beam block for annular illumination.

samples with a 1.4 N.A. oil-immersion objective (UPLSAPO 100XO, Olympus). To obtain a dark-field illumination, the central part of the light beam was blocked. The scattered light was collected with a 0.3 N.A. objective (UPLFLN 10X2, Olympus) and subsequently focused onto a 50 μm diameter pinhole before the spectrometer (AvaSpec-3648-USB2, Avantes). The effective area on the sample plane from which light was collected was estimated to be a 5 μm diameter circle, hence completely encompassing the full nanostructure. Spectra were typically acquired in 5 s to allow the detector to accumulate enough signal. The scattering spectra are normalized to the system response retrieved by removing the beam block (bright field illumination) to remove the inherent wavelength dependence of the white light source.

Numerical results were obtained using finite difference time domain (FDTD, Lumerical Solutions Inc.) calculations. For this, a total-field scattered-field (TFSF) plane wave source with

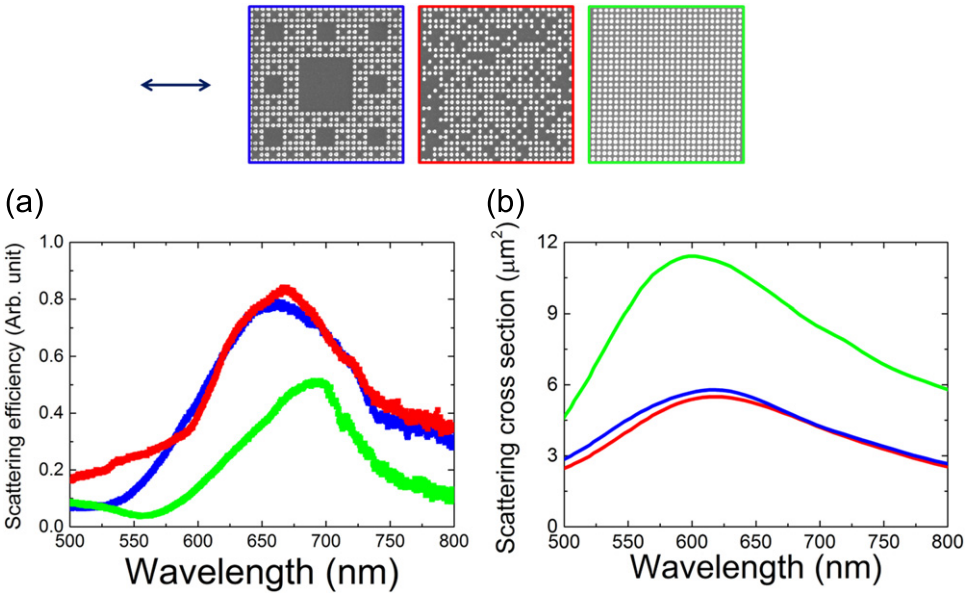

Figure 5. Measurement results (a) and numerical simulations (b) of the scattering efficiency of the Sierpinski carpet (blue), pseudo-random (red) and periodic (green) gold nanostructures. The double arrow indicates the polarization direction of the incident light. After subtraction of the background scattering signal arising from the glass substrate near the nanostructures, the scattering spectra are normalized by the bright-field illumination signal in order to remove the inherent wavelength dependence of the illuminating lamp.

normal incidence on the gold nanostructures was used as an excitation source. The mesh size in the simulation is 2 nm, and we use 'conformal variant 0' for the mesh refinement. The structures were composed of gold cylinders; the dielectric function of gold and glass are from references [24] and [25], respectively.

Results and discussions

To assess the broadband response of the Sierpinski carpet optical antenna, we determine its scattering spectrum in the visible and near-infrared wavelength regions. In figure 5 both measurement (a) and simulation (b) results are presented. Experimental results reveal a broad signal that peaks at ~660 nm, which is close to the result found in the numerical simulations. To determine whether this spectral response is due to the Sierpinski carpet morphology or just due to many monomers in close proximity, we also explore the pseudo-random and periodic structures. The former shows little difference; however, the scattering spectrum of the periodic nanostructure is red-shifted, now peaking at ~690 nm. Although all three morphologies produce a broadband scattering response, the periodic one shows the lowest efficiency for the measured spectrum, while the simulation indicates much higher scattering efficiency than the Sierpinski carpet and pseudo-random nanostructures. Also notice that in the measured spectra, the peak of the scattering spectrum of the periodic nanostructure has a red shift compared with the Sierpinski carpet and pseudo-random gold nanostructures but a blue shift in simulated results. These discrepancies arise from the exclusion of the 0th diffraction in the dark field configuration

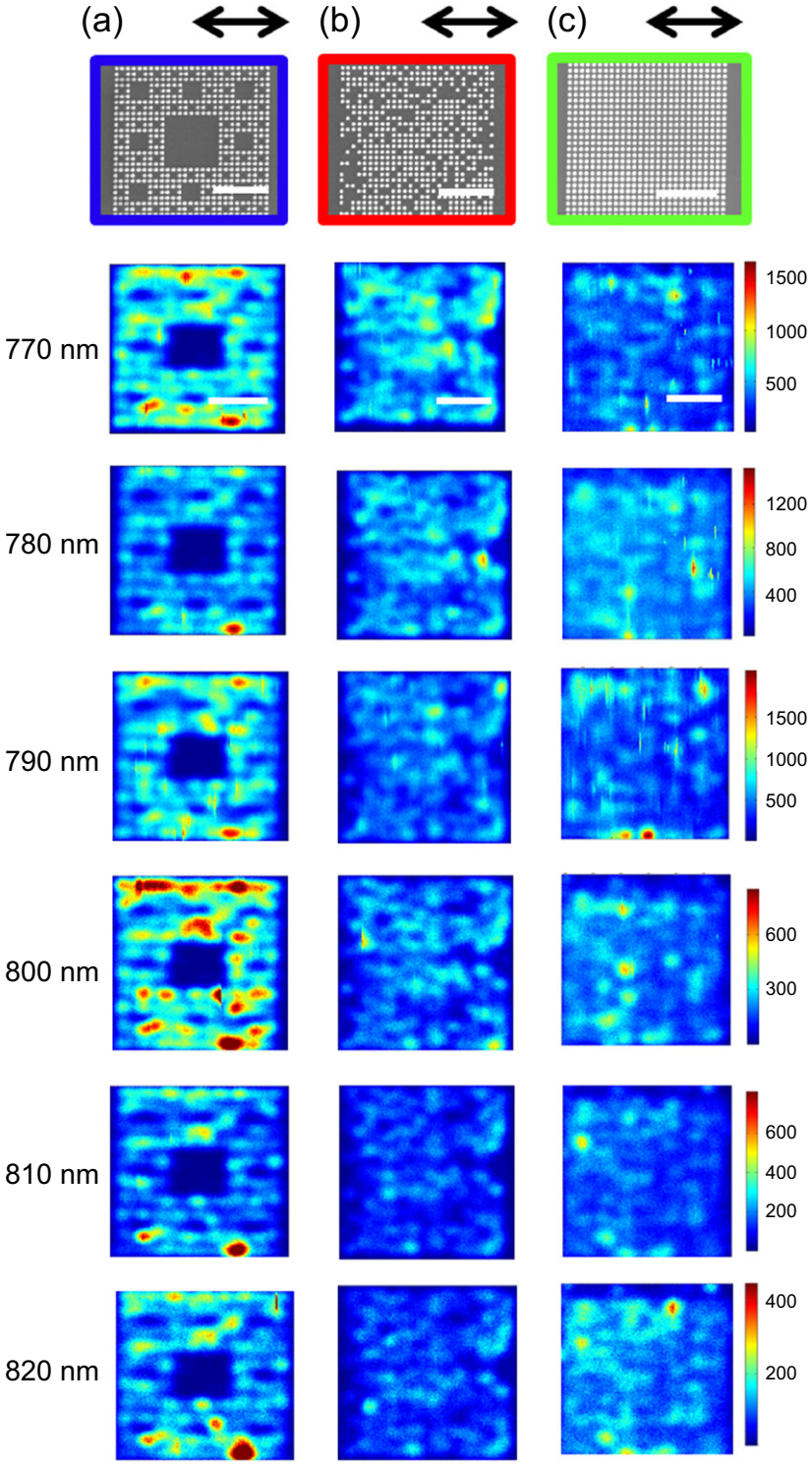

Figure 6. SEM and TPPL images of (a) Sierpinski carpet, (b) pseudo-random and (c) periodic gold nanostructures at an excitation wavelength of 770, 780, 790, 800, 810 and 820 nm. The double arrow indicates the direction of polarization of the excitation beam. The color bar indicates the number of counts collected for a scanning rate of 2.5 msec/pixel. The excitation power is around 1 mW for all samples. All white scale bar are 1 μm.

of experimental setup, whereas the simulation includes all scattered light. With a higher monomer number (729 for the periodic and 512 for the Sierpinski carpet and pseudo-random nanostructures), the periodic nanostructure has higher 0th diffraction, resulting in a higher scattering efficiency in the simulation result.

Near-field intensity measurements and numerical calculation

Methods

In the plasmonics research field, TPPL has been widely used for mapping hot spots of gold nanostructures spatially and spectrally [26] and for the measurement of intensity enhancement of gold bowtie optical antennas [27]. Recently TPPL was used to reveal the surface plasmon local density of states in thin single-crystalline triangular gold nanoprisms [28]. When focusing a near-infrared intense pulsed laser beam on gold, electrons in the valence d band absorb two photons for the transition to the conduction sp band. In this process, which is still actively studied, intraband transitions in the sp band can play a role [29, 30]. The sensitivity of TPPL to the high electric field enhancements that occur locally at gold nanostructures is generally attributed to its absorption of multiple photons that will be nonlinearly dependent on pump power. We use TPPL microscopy to estimate the near-field intensity enhancements of the Sierpinski carpet, pseudo-random, and periodic optical antennas.

To perform TPPL confocal microscopy, we used a mode-locked pulsed laser (Micra, Coherent Inc.) with a tunable wavelength from 750–830 nm and a pulse bandwidth ~5 nm. The pulse duration is several hundred femto-seconds. The beam is sent into an inverted microscope (IX71, Olympus) and directed by a dichroic mirror (700 nm dichroic short-pass filter, Edmund Optics) into the objective (UPLSAPO 100XO, Olympus). Samples are placed on a piezo scanning stage and moved relative to the focused excitation beam spot for scanning. The generated TPPL is collected by the same objective used for focusing the excitation beam, and the collected light is short pass filtered (FF01-694/SP, SEMROCK) to reject the excitation light. We thus only collect the visible wavelength contribution of the TPPL. The luminescent signal is focused onto a pinhole before a single-photon counting avalanche photodiode (Perkin-Elmer). Because all three samples are measured in sequence without changing the setup, the TPPL intensities can be directly compared.

To determine the near-field intensity enhancement of the Sierpinski carpet optical antenna, we record TPPL images as a function of excitation wavelength, which are further benchmarked by comparison to signals generated by the pseudo-random and periodic morphologies. As can be seen in figure 6, the intensity distribution of the TPPL counts roughly matches the morphology of the nanostructure; lower count numbers are generally correlated with a region with a lower density of monomers. Apart from this structural signature, a few 'hot spots' are visible, most notably in the TPPL images of the Sierpinski carpet and periodic nanostructures. These hot spots are not symmetrically distributed, as would be expected from the symmetry of the geometric patterns. In addition, the positions of the hot spots vary for different excitation wavelengths. Hence, we attribute these hot spots as arising from small defects due to the inevitable fabrication imperfections in the FIB milling.

To characterize the overall TPPL intensity generated by the nanostructures and determine the extent to which the hotspots contribute therein, we perform a histogram analysis of each image by plotting TPPL counts per pixel. As can be seen in figure 7, the signals arising from

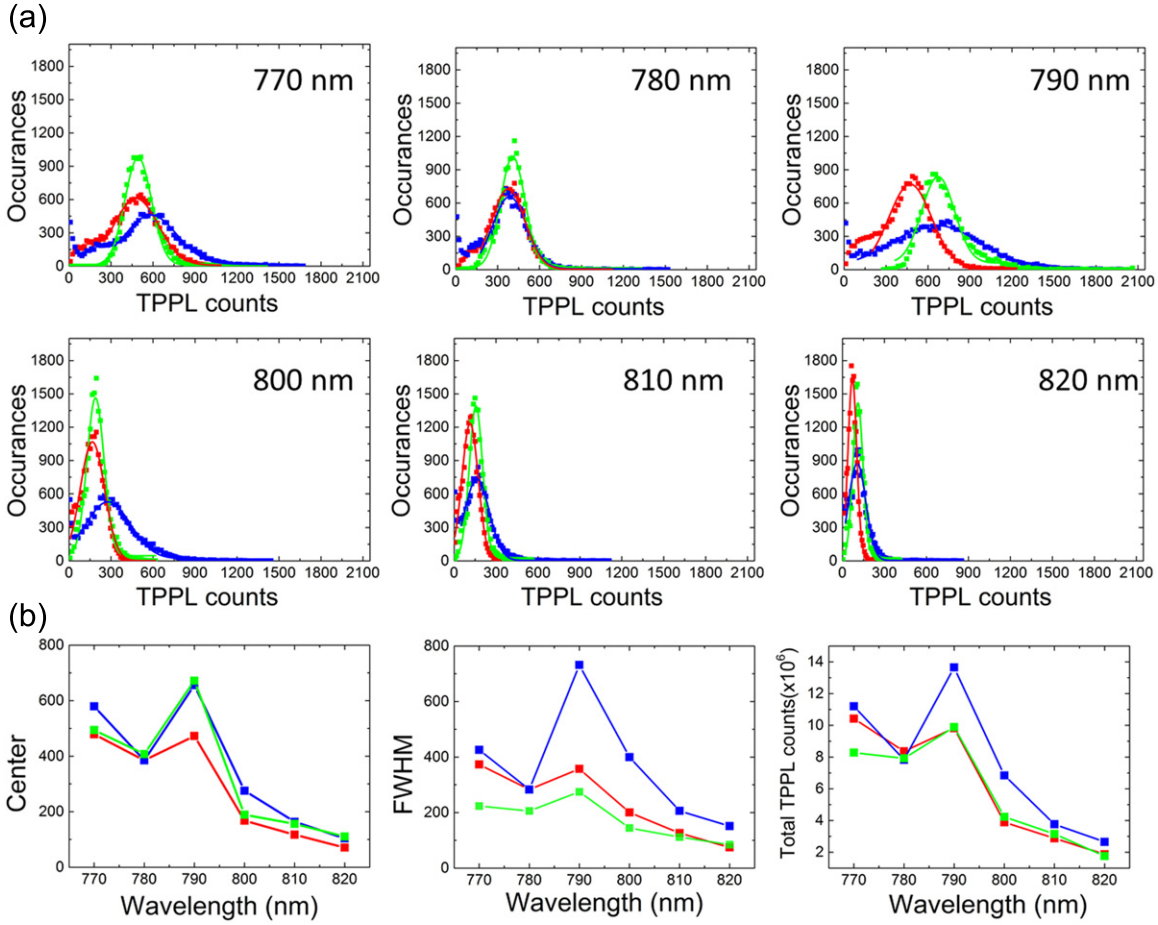

Figure 7. (a) Histograms of TPPL counts of the Sierpinski carpet (blue), pseudo-random (red) and periodic (green) gold nanostructures at excitation wavelength of 770, 780, 790, 800, 810 and 820 nm. (b) is the center and FWHM of Gaussian curve fitting of histogram, and total yields (from left to right) of TPPL counts of the Sierpinski carpet (blue), pseudo-random (red) and periodic (green) gold nanostructures.

regions containing hot spots are found in the long tail on the right side of the histogram and do not influence the central position and width of the main curve under which most intensity is found. figure 7(b) shows the center and full width at half maximum (FWHM) of a Gaussian curve fit to the TPPL count histogram for the Sierpinski carpet, pseudo-random, and periodic nanostructures at six excitation wavelengths. The total yield of TPPL intensity, constructed by integrating the total number of counts in the image, is also shown in figure 7(b), revealing a generally higher response for the Sierpinski carpet gold nanostructure. Note that despite the higher monomer count for the periodic nanostructure (729 vs 512 monomers), the Sierpinski carpet nanostructure has a higher total TPPL count.

To extract further quantitative measurements from TPPL images, we estimate the experimental TPPL intensity enhancement α_{exp} according to [31]:

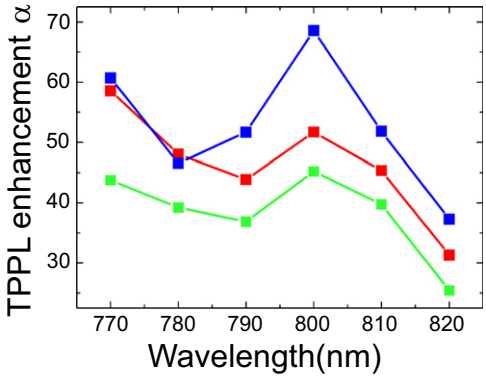

Figure 8. TPPL enhancement factor α of the Sierpinski carpet (blue), pseudo-random (red) and periodic (green) gold nanostructures.

$$\alpha_{\mathrm{exp}} = \sqrt{\frac{\left\langle TPPL_{\mathrm{sample}} \right\rangle \left\langle P_{\mathrm{film}} \right\rangle^2 A_{\mathrm{film}}}{\left\langle TPPL_{\mathrm{film}} \right\rangle \left\langle P_{\mathrm{sample}} \right\rangle^2 A_{\mathrm{sample}}}}, \tag{1}$$

where $<TPPL_{\mathrm{sample}}>$ and $<TPPL_{\mathrm{film}}>$ are the area-averaged signals from TPPL images of the gold nanostructure and a single crystalline gold film, respectively. Likewise, $<P_{\mathrm{sample}}>$ and $<P_{\mathrm{film}}>$ are the average powers of the excitation beams incident on the sample and the film, respectively. In our experiments, we used $<P_{\mathrm{sample}}> \sim 0.7$ mW and $<P_{\mathrm{film}}> \sim 7$ mW. Note that in our experiments the TPPL signal in the gold film and three nanostructures shows the same quadratic relation with excitation power. A_{film} and A_{sample} are the effective areas of the gold film and the gold nanostructure sample for generating TPPL, which is determined by the spot size of focused excitation laser and the area of gold, respectively. For simplicity, we set $A_{\mathrm{film}} = A_{\mathrm{sample}}$, which means that the calculated TPPL enhancement factor α will be underestimated [27].

Figure 8 shows the TPPL enhancement factor α calculated from equation (1). It features an interesting spectral behavior, falling off to low energy yet marked by a peak at 800 nm that is present in all three samples. Note that the response of an unstructured gold film (data not shown) is smooth without minima or maxima in this region. At 800 nm the measured α_{exp} of the Sierpinski carpet nanostructure is highest, reaching $\sim$70.

To determine whether the presence of hotspots has an influence on the enhancement factor, we recalculate α_{exp} following truncation of the high-intensity tails of the histograms. The effect is negligible: for the histogram of intensities from the Sierpinski carpet nanostructure obtained with excitation at 800 nm (figure 7(a)), truncating the tail at 900 TPPL counts yields an enhancement factor of 67, which is almost the same as the original value ($\alpha_{\mathrm{exp}} = 68$). For the periodic nanostructure, the enhancement factor upon truncation at 450 TPPL counts is identical to that found without truncation ($\alpha_{\mathrm{exp}} = 46$). Likewise for the pseudo-random nanostructure, the enhancement factor is unchanged after truncating the tail at 350 TPPL counts in the histogram. Even if we truncate the tail of the Sierpinski carpet gold nanostructure at 500 TPPL counts, i.e., well into the wing of the Gaussian curve, the value of α_{exp} is only reduced by 10%. Hence the presence of hot spots does not influence dramatically the estimation of α_{exp}.

Finally, to provide statistical significance to the observation of a higher enhancement factor α_{exp} for the Sierpinski carpet nanostructure, we determined the TPPL yields and corresponding enhancement factors for subunits of the nanostructures. This analysis, based on

the same data shown in figure 6, was performed on two structures, the Sierpinski carpet and the periodic array, by dividing the TPPL images into four equal quadrants. Due to symmetry considerations, the values of α_{exp} are expected to be the same in each quadrant; hence any variations can be attributed to imperfections of sample fabrication such as inhomogeneity of the gap size and shape of monomers. We found that for both samples, the variation in α_{exp} for the four quadrants was less than 10% of the value found for the entire sample area (figure 8). This result confirms the higher near-field intensity enhancement for the Sierpinski carpet nanostructure.

Conclusion

We characterized the Sierpinski carpet gold nanostructure, fabricated from single crystalline gold flakes, demonstrating its potential to serve as a broadband optical antenna. Dark-field scattering microscopy showed that the Sierpinski carpet morphology behaved in a manner similar to an arbitrarily chosen pseudo-random gold nanostructure. Furthermore, TPPL measurements showed that the Sierpinski carpet nanostructure has a near-field enhancement factor of 70 upon excitation with 800 nm light, which was more than 50% higher than the other two geometries studied. We tentatively attribute this intensity enhancement to the long-range order present in the Sierpinski carpet optical antenna. Based on these results, the Sierpinski carpet morphology is clearly an interesting antenna design to achieve broadband scattering response as well as high near-field enhancement. We cannot exclude the possibility that other pseudo-random morphologies may perform even better; however, given its easy implementation, we conclude that the 'self-similarity' of the fractal geometry provides a simple design principle and can serve as an initial morphology for further optimization on light-harvesting applications, e.g., by the particle swarm optimization algorithm or an evolutionary strategy [32, 33].

Acknowledgments

This research is financially supported by Nederlandse Organisatie voor Wetenschappelijk Onderzoek (NWO). The research of JLH is supported by an NWO-Vici grant; JCP acknowledges support from Stichting Technische Wetenschappen (STW) under the Nanoscopy program (project nr.12149).

References

[1] Barnes W L, Dereux A and Ebbesen T W 2003 Surface plasmon subwavelength optics *Nature* **424** 824–30
[2] Bohren C F and Huffman D R 1983 *Absorption and Scattering of Light by Small Particles* (New York: Wiley)
[3] Kreibig U and Vollmer M 1995 *Optical Properties of Metal Clusters* (New York: Springer)
[4] Teperik T V, García de Abajo F J, Borisov A G, Abdelsalam M, Bartlett P N, Sugawara Y and Baumberg J J 2008 Omnidirectional absorption in nanostructured metal surfaces *Nat. Photonics* **2** 299–301
[5] Catchpole K R and Polman A 2008 Plasmonic solar cells *Opt. Express* **16** 21793–800
[6] Knight M W, Sobhani H, Nordlander P and Halas N J 2011 Photodetection with active optical antennas *Science* **332** 702–4

[7] Tang L, Kocabas S E, Latif S, Okyay A K, Ly-Gagnon D-S, Saraswat K C and Miller D A B 2008 Nanometre-scale germanium photodetector enhanced by a near-infrared dipole antenna *Nat. Photonics* **2** 226–9
[8] Ferry V E, Verschuuren M A, Li H B T, Verhagen E, Walters R J, Schropp R E I, Atwater H A and Polman A 2010 Light trapping in ultrathin plasmonic solar cells *Opt. Express* **18** 237–45
[9] Nie S and Emroy S R 1997 Probing single molecules and single nanoparticles by surface-enhanced Raman scattering *Science* **275** 1102
[10] Bharadwaj P, Deutsch B and Novotny L 2009 Optical antennas *Adv. Opt. Photon.* **1** 438–83
[11] Novotny L and van Hulst N F 2011 Antennas for light *Nat. Photonics* **5** 83–90
[12] Ferry V E, Verschuuren M A, van Lare C, Walters R J, Schropp R E I, Atwater H A and Polman A 2011 Optimized spatial correlations for broadband light trapping in ultra-thin a-Si:H solar cells *Nano Lett.* **11** 4239–45
[13] Gopinath A, Boriskina S V, Feng N–N, Reinhard B M and Negro L D 2008 Photonic-plasmonic scattering resonances in deterministic aperiodic structures *Nano Lett.* **8** 2423–31
[14] Dallapiccola R, Gopinath A, Stellacci F and Negro L D 2008 Quasiperiodic distribution of plasmon modes in two-dimensional Fibonacci arrays of metal nanoparticles *Opt. Express* **16** 5544–55
[15] Dal Negro L and Boriskina S V 2012 Deterministic aperiodic nanostructures for photonics and plasmonics applications *Laser Photonics Rev.* **6** 178–218
[16] Hohlfeld R G and Cohen N 1999 Self-similarity and the geometric requirements for frequency independence in antennae *Fractals* **7** 79–84
[17] Sederberg S and Elezzabi A Y 2011 Sierpinski fractal plasmonic antenna: a fractal abstraction of the plasmonic bowtie antenna *Opt. Express* **19** 10456–61
[18] Volpe G, Volpe G and Quidant R 2011 Fractal plasmonics: subdiffraction focusing and broadband spectral response by a Sierpinski nanocarpet *Opt. Express* **19** 3612–8
[19] Zhu L-H, Shao M-R, Peng R-W, Fan R-H, Huang X-R and Wang M 2013 Broadband absorption and efficiency enhancement of an ultra-thin silicon solar cell with a plasmonic fractal *Opt. Express* **21** 313–23
[20] Mandelbrot B B 1982 *The Fractal Geometry of Nature* (San Francisco, CA: Freeman)
[21] Sierpinski W 1916 Sur une courbe cantorienne qui contient une image biunivoque et continue de toute courbe donnée *C. R. Hebd. Seanc. Acad. Sci.* **162** 629–32
[22] Huang J-S *et al* 2010 Atomically flat single-crystalline gold nanostructures for plasmonic nanocircuitry *Nat. Commun.* **1** 1–8
[23] Kan C, Zhu X and Wang G 2006 Single-crystalline gold microplates: synthesis, characterization, and thermal stability *J. Phys. Chem.* B **110** 4651–6
[24] Johnson P B and Christy R W 1972 Optical constants of the noble metals *Phys. Rev.* B **6** 4370–9
[25] Palik E D 1985 *Handbook of Optical Constants of Solids* (Orlando, FL: Academic)
[26] Ghenuche P, Cherukulappurath S, Taminiau T H, van Hulst N F and Quidant R 2008 Spectroscopic mode mapping of resonant plasmon nanoantennas *Phys. Rev. Lett.* **101** 116805–8
[27] Schuck P J, Fromm D P, Sundaramurthy A, Kino G S and Moerner W E 2005 Improving the mismatch between light and nanoscale objects with gold bowtie nanoantennas *Phys. Rev. Lett.* **94** 017402
[28] Viarbitskaya S, Teulle A, Marty R, Sharma J, Girard C, Arbouet A and Dujardin E 2013 Tailoring and imaging the plasmonic local density of states in crystalline nanoprisms *Nat. Mater.* **12** 426–32
[29] Beversluis M R, Bouhelier A and Novotny L 2003 Continuum generation from single gold nanostructures through near-field mediated intraband transitions *Phys. Rev.* B **68** 115433
[30] Biagioni P, Brida D, Huang J-S, Kern J, Duò L, Hecht B, Finazzi M and Cerullo G 2012 Dynamics of four-photon photoluminescence in gold nanoantennas *Nano Lett.* **12** 2941–7
[31] Hohenau A, Krenn J R, Garcia-Vidal F J, Rodrigo S G, Martin-Moreno L, Beermann J and Bozhevolnyi S I 2007 Spectroscopy and nonlinear microscopy of gold nanoparticle arrays on gold films *Phys. Rev.* B **75** 085104

[32] Forestiere C, Donelli M, Walsh G F, Zeni E, Miano G and Negro L D 2010 Particle-swarm optimization of broadband nanoplasmonic arrays *Opt. Lett.* **35** 133–5
[33] Donelli M 2013 Design of broadband metal nanosphere antenna arrays with a hybrid evolutionary algorithm *Opt. Lett.* **38** 401–3